# Thermospheric Nitric Oxide Cooling Responses to the December 14, 2020 Solar Eclipse

**Ningchao Wang[1], Wandi Yu[2], Jia Yue[3,4], Wenbin Wang[5], Liying Qian[5], Joseph M. Mclnerney[5], James M. Russell III[2], and Martin G. Mlynczak[1]**

[1]NASA Langley Research Center, Hampton, VA.

[2]Center for Atmospheric Sciences, Hampton University, Hampton, VA 23668.

[3]Catholic University of America, Washington DC.

[4]NASA Goddard Space Flight Center, Greenbelt, MD.

[5]High Altitude Observatory, National Center for Atmospheric Research, Boulder, CO.

Corresponding author: Ningchao Wang (ningchao.wang@nasa.gov)

**Key Points:**

- SABER observed a decrease in radiative cooling by NO in the thermosphere during the solar eclipse on December 14, 2020.
- The eclipse-induced NO cooling rate decrease observed by SABER is consistent with the WACCM-X simulation.
- The eclipse-time decreases of the NO concentration and temperature are the major drivers of the NO cooling rate decrease during the eclipse.

## Abstract

The behaviors of the nitric oxide (NO) cooling in the lower thermosphere during the December 14, 2020 solar eclipse are studied using SABER measurements and WACCM-X simulations. We found that NO cooling rate decreases during the solar eclipse in both SABER measurements and WACCM-X simulations. The maximum decrease of the NO cooling is 40% in SABER measurements and 25% in WACCM-X simulations. The NO cooling process is initiated almost entirely through the collisions with atomic oxygen (O) which depends linearly on NO and O densities and non-linearly on the neutral temperature. During the eclipse, the NO concentration and temperature decreases are larger than that of O concentration. Consequently, the eclipse-time NO concentration and temperature decreases are the major drivers of the NO cooling rate decrease. The decreases of the temperature and the NO concentration contribute comparably to the eclipse-time NO cooling rate decrease.



## Plain Language Summary

Sounding of the Atmosphere using Broadband Emission Radiometry (SABER) is an instrument on the Thermosphere Ionosphere Mesosphere Energetics and Dynamics satellite (TIMED) satellite which was launched on 7 December 2001. Whole Atmosphere Community Climate Model with Thermosphere and Ionosphere eXtension (WACCM-X) is the National Center for Atmospheric Research (NCAR) whole atmosphere global circulation model. In this work, we used SABER measurements and WACCM-X simulations to investigate the behaviors of the NO cooling during the December 14, 2020 solar eclipse. The NO cooling decreases during the eclipse from both the SABER observations and WACCM-X simulations. The decrease of the NO cooling is mostly caused by the decreases of the NO density and temperature during the solar eclipse.


## 1 Introduction

During solar eclipses, the reduction of solar radiation in the moon shadow reduces photoionization, photodissociation, and heating in the upper atmosphere, which in turn initiates changes in dynamics and chemistry (Barth, 1992; Dobbin et al., 2006; Duff et al., 2003; Aplin et al., 2016). Previous studies found significant solar eclipse induced temperature reductions (up to 30 K) in the upper atmosphere, and the temperature change is global due to solar eclipse excited

wave transport (Dang et al., 2018; Lei et al., 2018; McInerney et al., 2018). NO infrared cooling serves as a thermostat in the upper atmosphere, which is sensitive to the temperature variations induced by the transient space weather events such as solar flares and geomagnetic storms (Mlynczak et al., 2003, 2005). NO emission has much larger variations on shorter timescales and dominates the thermospheric cooling process (Lu et al., 2010; Mlynczak et al., 2003, 2005, 2007, 2010). There are extensive studies focused on NO density and NO infrared cooling responses to geomagnetic storms (e.g., Barth et al., 2009; Barth, 2010; Bharti et al., 2018; Dobbin et al., 2006; Knipp et al., 2017; Lei et al., 2011, 2012; Li et al., 2019; Lu et al., 2010; Mlynczak et al., 2003, 2005, 2007; Richards, 2004; Sheng et al., 2017; Siskind et al., 1989; Zhang et al., 2014), however, the changes of NO concentration and NO infrared cooling during transient solar eclipse events have never been directly observed until now.

Moreover, it is not clear how NO cooling responds to the eclipse-driven temperature change, as well as how solar eclipse driven dynamical and chemical changes impact NO cooling locally. The production, transport, and loss of NO depend on solar radiation level, global circulation, and temperature structures of the upper atmosphere (Barth, 1992; Dobbin et al., 2006; Duff et al., 2003), all of which are expected to change during the transient solar eclipse events (Aplin et al., 2016). On the other hand, NO cooling feeds back to the total energy budget and affects the state of the upper atmosphere (Mlynczak et al., 2003, 2005, 2007). This full chain of NO-associated dynamic and chemical processes during solar eclipses, however, has not been understood.

In this paper, we will use the measurements of the Sounding of the Atmosphere using Broadband Emission Radiometry (SABER) onboard the Thermosphere Ionosphere Mesosphere Energetics and Dynamics satellite (TIMED) satellite to investigate how the NO cooling in the mesosphere and lower thermosphere region responds to the solar eclipse on December 14, 2020. In addition, we will use the National Center for Atmospheric Research (NCAR) Whole Atmosphere Community Climate Model with Thermosphere and Ionosphere eXtension (WACCM-X) to assist our investigation. The WACCM-X is integrated the ‘eclipse mode’ that will be used to produce a model comparison with the SABER observation.

We will examine the impact of the solar eclipse on the atmospheric concentration and temperature, as well as the NO cooling to address the following questions: (1) how does SABER

observed NO cooling respond to the December 14, 2020 solar eclipse? (2) are the SABER NO cooling variations consistent with numerical simulations? and (3) what are the mechanisms governing the NO cooling rate change during the eclipse? The paper is organized as follows: a brief introduction of the solar eclipse on December 14, 2020, and descriptions of the TIMED SABER NO cooling data and WACCM-X simulations are summarized in section 2; the methods are discussed in section 3; the results and discussions are presented in section 4 followed by a brief summary in section 5.

## 2 Background

### 2.1 Solar Eclipse on December 14, 2020 and SABER TIMED NO cooling observation

The Solar eclipse traversed the mid-latitude South America from the west to east on December 14, 2020. The total eclipse started over the east Pacific Ocean at 14:32 UT and ended over the east coast of Africa at 17:54 UT. The penumbral shadow (partial eclipse) touched the Earth at 13:33 UT over the Pacific Ocean, and disappeared at 18:53 UT. The path of the totality is shown as the blue line in Figure 1.

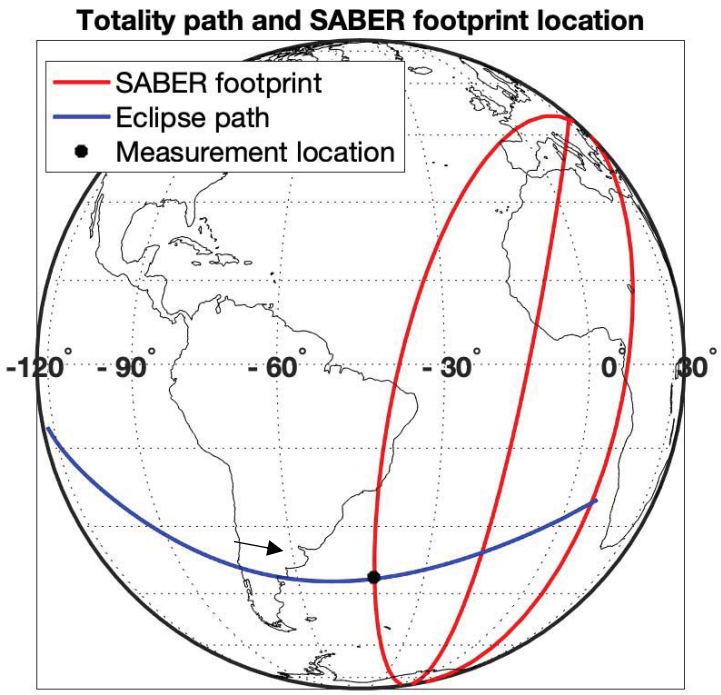


**Figure 1**. The path of the totality for the solar eclipse on December 14, 2020 (blue line) and the SABER foot print during the solar eclipse (red lines). The SABER foot print passed through the totality region at 17:58 UT at (41° W, 42° S), labeled as a black star. The black arrow denotes the traverse direction of the totality.

The SABER instrument is on-board the NASA TIMED satellite which was launched on 7 December 2001 into a 74.1° inclination orbit at 630 km altitude with a period of ~1.6 hours (Russell et al., 1999). The latitude coverage shifts between 83° N–53° S and 53° N–83° S, due to a ~60 days yaw cycle of the satellite. The SABER infrared sensor performs limb scans in 10

distinct spectral channels with about 1400 radiance profiles a day. The spectral coverage of the instrument is from 1.27 to 15.4 μm (Mlynczak, 1997, 2005, 2007), including NO infrared emission at 5.3 μm (Kockarts, 1980), which is used to derive the NO cooling rate (Mlynczak et al., 2010, 2021) in the unit of watts/$m^3$. The SABER cooling rates are reported in the unit of watts/$m^3$ due to the absence of simultaneous temperature and pressure data (to obtain total number density) in the lower thermosphere required to express the rate in K/day.

The SABER latitude coverage during the December 14, 2020 solar eclipse is 53° N–83° S, which covers the totality path. The footprint of the SABER measurement is shown as red lines in Figure 1, which is crossing the South Atlantic Anomaly (SAA). However, there is no evidence that the SAA impacts the SABER data. Since the SABER instrument scans the Earth limb from 400 km to the Earth surface in ~ 1 minute, during which the TIMED satellite traveling ~ 4 degrees in latitude. For the altitude range of 100 -200 km, the change in latitude during the SABER instrument scan would be less than 1 degree, thus the geographical extent of the observation volume will not affect the conclusions. The black star marks the SABER foot print that passes through the totality path at (41° W, 42° S) for the first time at 17:58 UT which is 50 minutes after the totality occurred and 10 minutes after the eclipse disappeared. Thus, the SABER measurement was in the recovery phase of the solar eclipse. The observation location had been in shadow for ~ 100 minutes. NO cooling rate is analyzed to examine responses of the NO cooling rate to the December 2020 solar eclipse.

### 2.2 WACCM-X

The WACCM-X is a self-consistent 3-D whole atmosphere global circulation model and a configuration of the NCAR Community Earth System Model (CESM) (Hurrell et al., 2013; Liu et al., 2018; Liu et al., 2018). WACCM-X has a standard resolution that is 1.9° × 2.5° (latitude × longitude) and a finer resolution of 0.95° × 1.25°, and 0.25 scale height in the vertical above 1 hPa (~50 km) from the surface to ~500-700 km depending on solar activity (Liu et al., 2018). The finer resolution is applied in this work. WACCM-X chemistry is based on the Model for Ozone and Related Chemical Tracers (MOZART) (Kinnison et al., 2007), which includes all of the chemical reactions that are important for the middle and upper atmosphere.

The calculation method of the eclipse induced solar radiation variations developed by Curto et al., (2006) and Le et al., (2008) has been implemented in the WACCM-X to conduct the solar eclipse simulations. Under the eclipse mode, an eclipse factor function is calculated as the ratio of the Sun masked by the Moon, and the eclipse-time solar radiation is the solar radiation flux multiplied by this eclipse factor function. More details about eclipse mode in WACCM-X can be found in (Dang et al., 2018; McInerney et al., 2018 and references therein).

## 3 Methods

In this work, we first compare the NO cooling rate during the eclipse and the non-eclipse reference from the SABER measurements. As shown in Figure 1, the measurements of the NO cooling rate during the eclipse are taken at 17:58 UT at (41° W, 42° S). To compute the non-eclipse reference, we identify the SABER measurements at the similar local time (within 30 minutes) and adjacent location (within 10 degrees in both latitude and longitude) as the eclipse time measurement position within 3 days before the eclipse (December 11 to 13, 2020). During these days, F10.7 is around 80 sfu and Kp is smaller than 2. The average value of the 9 NO cooling measurements from the reference days will be used as the non-eclipse reference. The NO cooling rate changes will be determined by comparing data obtained during the eclipse with the non-eclipse reference data. Since the reference is within 3 days of the eclipse time, and the geomagnetic condition is similar to the eclipse time during these days, the atmosphere state during the reference period is close to that during the eclipse.

WACCM-X simulations are compared to the SABER observed NO cooling variation. To simulate the effects of the eclipse using WACCM-X, we first perform a model spin-up, with initial conditions from 1 December 2019 with realistic Kp and F10.7, and run for 20 days up to the beginning of the eclipse day. A baseline simulation without solar eclipse is then performed, starting from the end of the spin-up run. Two masks are used together in the eclipse simulation: an “unscaled” mask with an effective solar radius of 1.0, representative of infrared, visible, and near-ultraviolet fluxes, and a “scaled” mask for the extreme-ultraviolet (EUV) spectral region, using an effective solar radius of 1.125 (Huba & Drob, 2017). The simulated NO cooling rate change is determined by comparing outputs of the WACCM-X solar eclipse simulations with the baseline simulations.

The NO cooling rate in the WACCM-X is calculated based on Kockarts (1980). The details of the equation can be found in (Kockarts, 1980; Sheng et al., 2017 and the references there in) and is given by this equation :

$$\boldsymbol{NO\ Cooling\ Rate} = \frac{\boldsymbol{h\nu_0 A_{10} n(NO_{v=0}) \times (k_O n(O) + k_{O_2} n(O_2))}}{\boldsymbol{k_O n(O) + k_{O_2} n(O_2) + A_{10}}} \times \boldsymbol{e}^{-\frac{\boldsymbol{h\nu_0}}{\boldsymbol{k_B T_N}}} \qquad (1)$$

where $h$ is Planck's constant; $\nu_0 = c/5.3\mu m$ where $c$ is the speed of light; $A_{10}$ is 13.3 $s^{-1}$ representing the transition probability of $NO(v = 1) \rightarrow NO(v = 0) + h\nu_{5.3\mu m}$; $n(NO_{v=0})$, $n(O), n(O_2)$ are number densities of $NO_{v=0}, O, O_2$, resepectively; $k_O$ is set to be 4.2× $10^{-11}\ cm^3 s^{-1}$ (Hwang et al., 2003) which is the vibrational relaxation rate of $NO(v = 1)$ by collisions with O; $k_{O_2}$ is set to be 2.4× $10^{-14}\ cm^3 s^{-1}$ (Murphy et al., 1975), which stands for the vibrational relaxation rate of $NO(v = 1)$ by collisions with $O_2$; $k_B$ is Boltzmann's constant, and $T_N$ is neutral temperature. As shown in Eq. (1), NO cooling rate is a function of the NO concentration, the O concentration, the $O_2$ concentration, and temperature (Kockarts, 1980; Mlynczak et al., 2005), all of which are expected to change during the transient solar eclipse event. The cooling process is initiated by the collision between O, and NO and $O_2$ and NO, which depends linearly on the O, $O_2$, and NO amounts and non-linearly on the neutral kinetic temperature. The cooling process excited by $O_2$ is no more than 0.03% of that excited by O, thus, $O_2$ is not a significant excitation source relative to O. To identify the mechanisms that cause NO cooling variation during the eclipse, we investigate the variations of NO and atomic O concentrations, and temperature during the solar eclipse with WACCM-X simulations.

## 4 Results and Discussions

### 4.1 NO cooling rate difference during the eclipse from SABER measurements

The infrared radiation emission from NO at 5.3 μm cools the Earth's lower and middle thermosphere from 100 km to 250 km, which can be measured by the SABER instrument. However, below 115 km, the SABER NO cooling measurements represent the competition between the radiative excitation and collisions to excite NO, thus, are not representative of

radiative cooling (Mlynczak et al., 2021). In this work, we show the NO cooling rate above 115 km.

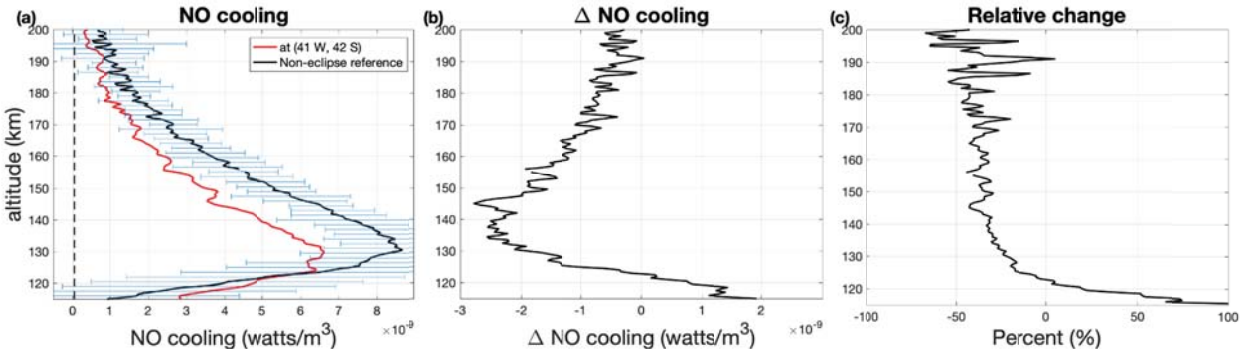


**Figure 2**. (a) Vertical profile of the NO cooling rate in units of watts/m$^3$ during December 14, 2020 solar eclipse (red) at 17:58 UT at (41° W, 42° S) and non-eclipse reference (black), derived from the SABER measurements. The equivalent noise value for the cooling rate is shown as the black dashed line. The horizontal bars represent the second standard deviation ($2$-$\sigma$) of the non-eclipse means; (b) the difference of the NO cooling rate between the eclipse and the non-eclipse reference; (c) the relative change of the NO cooling during the eclipse with respect to the non-eclipse reference.

Figure 2(a) shows the SABER NO cooling rate during the solar eclipse on December 14, 2020 in the lower thermosphere from 115 km to 200 km. The vertical profile of NO cooling rate in the eclipse region is shown in red, and the non-eclipse reference is shown in black. The horizontal bars represent the second standard deviation of the non-eclipse measurements. The NO cooling rate increases from 115 km to 130 km, and decreases above 130 km before and during the solar eclipse. During the eclipse, the NO cooling rate increases from $2.9 \times 10^{-9}$ watts/m$^3$ at 115 km to $6.5 \times 10^{-9}$ watts/m$^3$ at 130 km. Above 130 km, the NO cooling rate decreases from $6.5 \times 10^{-9}$ to $0.4 \times 10^{-9}$ watts/m$^3$ with increasing altitude. For the non-eclipse reference, the NO cooling rate increases from $1 \times 10^{-9}$ watts/m$^3$ at 115 km to $8.5 \times 10^{-9}$ watts/m$^3$ at 130 km. Above 130 km, the NO cooling rate decreases from $8.5 \times 10^{-9}$ to $0.6 \times 10^{-9}$ watts/m$^3$ with increasing altitude. Below 122 km, the NO cooling rate is larger during solar eclipse than the non-eclipse reference. while above 122 km, the NO cooling rate is smaller relative to the non-eclipse reference. Below 130 km the eclipse time NO cooling rate (red line) is within the variability ($2$-$\sigma$) of the non-eclipse reference, indicating that the eclipse time NO cooling rates between 115 and 130 km may be influenced by a combination of the atmospheric variability and

the solar eclipse. In the altitude range between 130 km and 180 km, the NO cooling during the solar eclipse is outside of the range of the 2-σ standard deviation of the non-eclipse reference. Thus, there is more than 95% likelihood that the eclipse time NO cooling variation with respect to the non-eclipse reference is not associated with the atmospheric variability. In addition, the SABER single profile random noise for the NO cooling rate is ~ $4.7 \times 10^{-11}$ watts/m$^3$ marked as the vertical dashed line in Figure 2(a), which is 2 orders of magnitude smaller than the NO cooling rate below 180 km. Thus, the measurement noise is negligible and will not affect our conclusion.

Figure 2(b) shows the NO cooling rate difference between the eclipse time and non-eclipse reference. From 122 km to 145 km, the difference of the NO cooling rate increases with increasing altitude, while above 145 km, the eclipse-induced difference of the NO cooling rate decreases with increasing altitude. The peak change of the NO cooling rate is $-2.8 \times 10^{-9}$ watts/m$^3$ at 145 km, which is nearly a 40% decrease with respect to the reference. Figure 2(c) shows the relative change of the eclipse time NO cooling with respect to the non-eclipse reference, which is compute as the ((NO cooling eclipse – NO cooling reference)/NO cooling reference). The relative change is positive below 122 km, while it is negative above 122 km. Between 130 km and 180 km, the relative change varies between -20% and -40%. Above 180 km, the variation of the NO cooling relative change is large, which is probably effects of the measurement random noise since the measured radiance gets close to the noise level at high altitudes as shown in Figure 2(a).

### 4.2 NO cooling rate difference during the solar eclipse simulated by WACCM-X

To help understand the observation results, we used WACCM-X to simulate the December 14, 2020 solar eclipse and compared the solar eclipse simulations with the non-eclipse simulations.

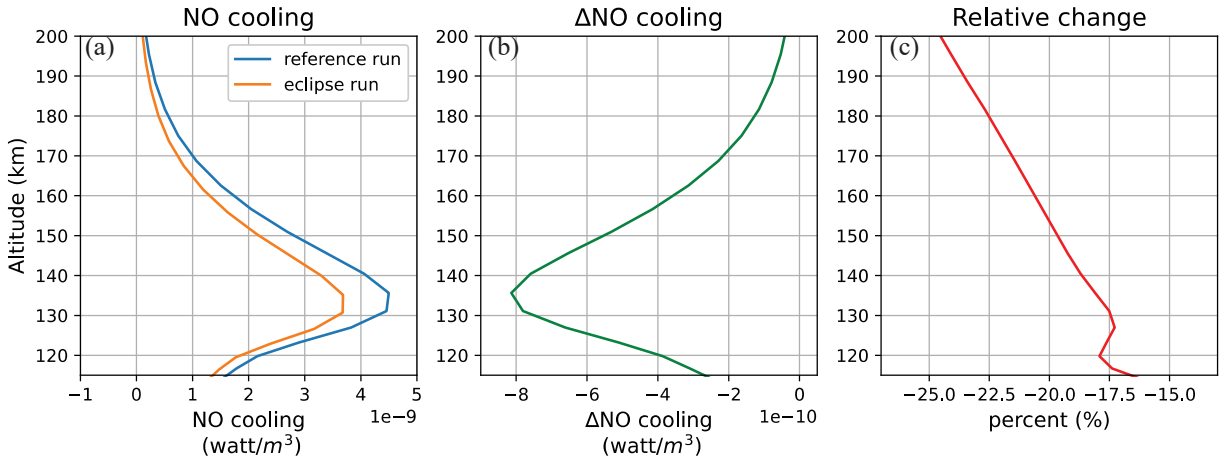


228

229 **Figure 3**. WACCM-X simulations for the December 14, 2020 solar eclipse at 17:58 UT and at (41° W, 42° S).
230 (a) NO cooling rate with eclipse simulations shown in orange and non-eclipse reference shown in blue; (b) the
231 difference of the NO cooling power between during the eclipse and the non-eclipse reference; (c) the relative
232 change of the NO cooling power with respect to the non-eclipse reference.

233 Figure 3(a) shows the simulated NO cooling vertical profile during the eclipse (orange line) and
234 non-eclipse reference (blue line). The magnitude of the NO cooling change during the eclipse
235 and the relative change of NO cooling with respect to the non-eclipse reference are shown in
236 Figures 3(b) and 3(c), respectively. In Figure 3(a), the NO cooling rates for both the eclipse
237 simulation and non-eclipse reference increase from 115 km to 135 km, and decrease from 135
238 km to 200 km, which is analogous to the SABER measurements. During the solar eclipse, the
239 simulated NO cooling rate becomes smaller. The magnitude of the change of NO cooling rate
240 increases from $3 \times 10^{-10}\ watts/m^3$ at 115 km to $8 \times 10^{-10}\ watts/m^3$ at 135 km, then the
241 NO cooling rate decreases to $\sim 1 \times 10^{-10}\ watts/m^3$ with increasing altitude (Figure 3(b)).
242 The relative change shown in Figure 3(c) varies between -17% and -25%.

243 The vertical profile of the simulated NO cooling rate is similar to the SABER measurement for
244 both during the eclipse-time and non-eclipse reference, as the NO cooling rates increase from
245 115 km to ~ 130km, then decrease with altitude above 130 km. Since both SABER measured and
246 WACCM-X simulated NO cooling rates are at the same order ($10^{-9}\ watts/m^3$), and have
247 similar trend in the vertical profiles, the difference of the NO cooling rate between the SABER
248 measurements and WACCM-X simulations will not impair our conclusion. Above 130 km, the

NO cooling rate during the eclipse becomes smaller compared to the non-eclipse reference for both the SABER observations and the WACCM-X simulations, which indicates that the solar eclipse reduces the NO cooling rate in the lower thermosphere. In summary, WACCM-X simulations show that a solar eclipse can induce NO cooling rate changes, which are large enough to be readily observable by SABER.

Moreover, the peak NO cooling rate change (maximum difference between the eclipse-time NO cooling rate and the non-eclipse reference) derived from the SABER data appears at a higher altitude (at 145 km) than the WACCM-X simulated results (at 135 km). The possible reasons for this are the day-to-day variation of the geospace environment. For example, the non-eclipse reference for the SABER measurements is defined as the average NO cooling rate profile at the similar local time and location as the eclipse time measurement, the approach cannot account for effects such as geomagnetic activity, tidal variability, or dynamical effects. At 12:00 UT on December 14, there is a small disturbance in the AE index of ~250 nT. Since the NO cooling rate is sensitive to geomagnetic activity, this small disturbance might cause the NO cooling rate variation during the solar eclipse (Mlynczak et al., 2003; 2005), and consequently may contribute to the difference between the SABER measurements and WACCM-X simulations. Additionally, the model may over/under estimate the NO cooling rate as well. As a climate model, WACCM-X cannot be expected to accurately simulate a single event. Thus, in this work, we do not expect that the WACCM-X simulations could perfectly match the observations. We intend to show the analogue behavior of the eclipse-time NO cooling rate in both SABER observations and WACCM-X simulations, which would be the evidence of the solar eclipse effect.

### 4.3 The driving mechanisms of the eclipse-time NO cooling rate difference

As mentioned above, to investigate the driving mechanism of the NO cooling rate difference induced by the solar eclipse, we need to examine the behaviors of concentrations of NO and O, and temperature during the eclipse. Since SABER does not provide those measurements above 115 km, we use WACCM-X simulations to conduct this investigation.

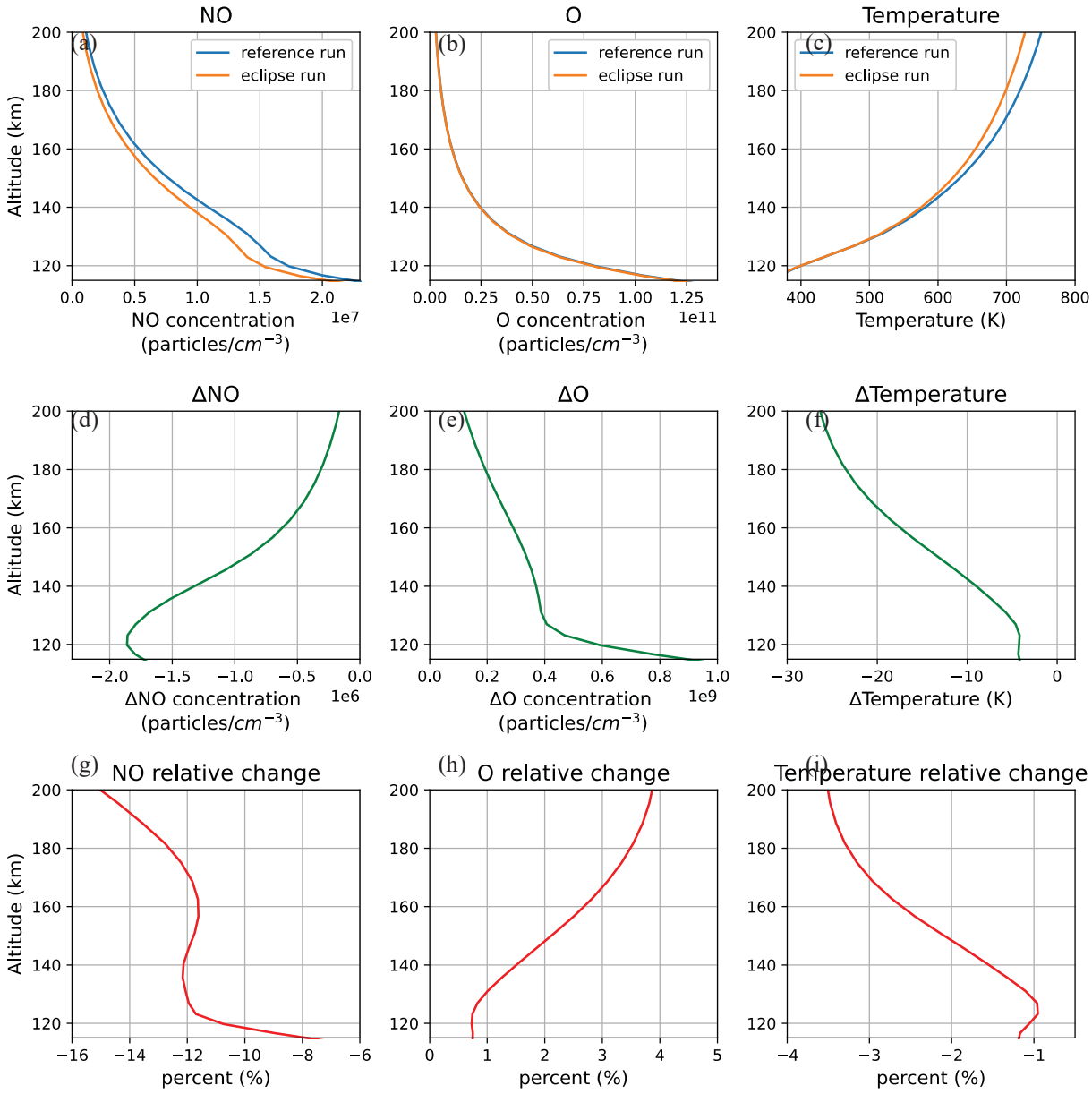


**Figure 4**. WACCM-X simulations for the December 14, 2020 solar eclipse at 17:58 UT and at (41° W, 42° S). The results from the solar eclipse and non-eclipse reference simulations are shown as orange and blue lines, respectively, in the top row for (a) NO concentration, (b) O concentration, and (c) temperature. The differences between the eclipse and non-eclipse simulations are shown in the middle row for (d) ΔNO concentration, (e) ΔO concentration, and (f) ΔT. The corresponded relative change with respect to the non-eclipse reference are shown in the bottom row for (g) NO concentration, (h) O concentration, and (i) temperature.

Figure 4 shows the vertical profiles of (a) NO concentration, (b) atomic O concentration, and (c) temperature during solar eclipse (orange line) and non-eclipse reference (blue line) on the top

284 row. The corresponding differences between eclipse result and non-eclipse reference (d-f) and
285 the relative change with respect to the non-eclipse reference (g-i) are shown in the middle row
286 and bottom row, respectively.

287 As shown in Figures 4(a) and 4(c), during the eclipse, the NO concentration and temperature are
288 smaller comparing to the non-eclipse references, while the change of O concentration is
289 extremely small as shown in Figure 4(b), and the relative change of the O concentration is up to
290 4%. Since NO cooling quasi-linearly depends on the O concentration, thus the O variation is of
291 little consequence.

292 We also investigated the spatial and temporal distribution of the NO cooling, NO concentration
293 and temperature during solar eclipse.

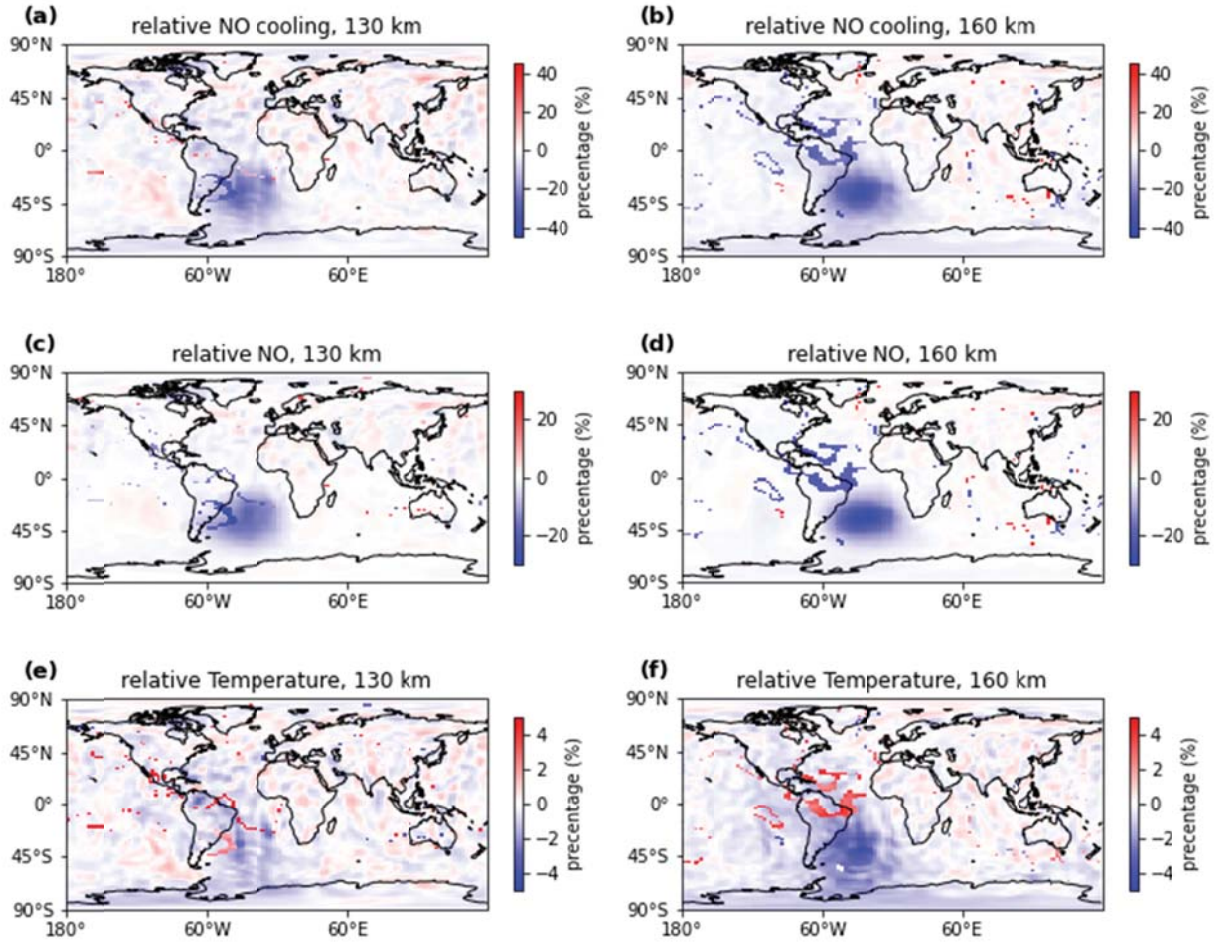


294

**Figure 5**. The spatial distribution of (a-b) NO cooling relative change, (c-d) NO density relative change, and (e-f) temperature relative change with respective to the non-eclipse reference at 17:58 UT at 130 km (left) and at 160 km (right). In each panel, pixel color represents the relative change in percent.

Figure 5 shows the global distribution of the NO cooling, NO concentration and temperature relative change during solar eclipse with respect to the non-eclipse reference at 130 km and 160 km, respectively. There are significant changes in NO cooling, NO concentration and temperature in the area where the totality occurs. Thus, the solar eclipse could affect the NO cooling by causing the decreases of the NO concentration and temperature.

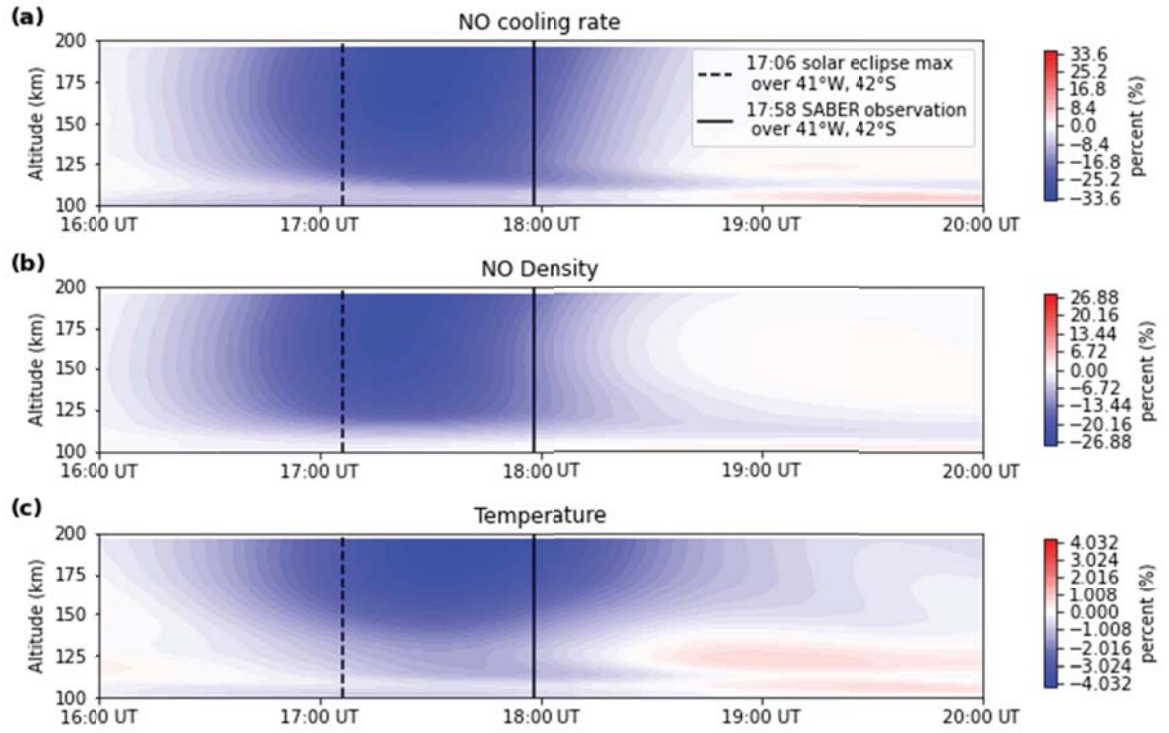


**Figure 6**. The relative change of the simulated (a) NO cooling, (b) NO density, and (c) temperature with respect to the non-eclipse reference simulations for the December 14, 2020 solar eclipse from 16:00 UT to 20:00 UT at (41° W, 42° S). In each panel, x-axis represents the universal time, and y-axis represents altitude. Pixel color represents the relative change in percent. The vertical dashed line marks the time of the totality occurred over (41° W, 42° S), and the solid vertical line marks the time when SABER observation is available at this location. The dotted line marks the time of the maximum relative change.

Figure 6 shows the temporal revolution of (a) NO cooling, (b) NO concentration, and (c) temperature at (41° W, 42° S). Pixel colors represent the relative changes. The vertical dashed

line marks the time of the totality occurred over (41° W, 42° S), and the solid vertical line marks the time when SABER observation is available at this location. As shown in Figure 6, the NO density relative change reaches the maximum (-26%) first at 17:15 UT, and the NO cooling relative change maximizes at 17:20 UT (-33%). The decreases of NO cooling rate and NO concentration during solar eclipse occur simultaneously, and both of them have a fast response at the beginning of the totality (10-15 minutes after the totality on site), which argues that the decrease in NO concentration is a main driver that cause the NO cooling decrease during the solar eclipse. The temperature also decreases after the totality, but reaches its maximum change (-4%) at 17:40 UT. Since NO cooling serves as the 'thermostat' of the upper atmosphere, temperature variations will cause the change in NO cooling as shown in Eq. (1). Moreover, the temperature at ~ 130 km increases after 18:30 UT. This temperature variation may not relate to the solar eclipse since this temperature change occurs ~ 40 minutes after the solar eclipse end at that location.

The most significant chemical processes related to NO production (Eqs. (2-4)), radiative cooling processes (Eqs. (5a-c)), and destruction (Eq. (6)) in the upper atmosphere are listed below (Barth, 1992; Dobbin et al., 2006; Richards, 2004; Sharma et al., 1998):

$$e^* + N_2 \rightarrow N(^2D) + N(^4S) + e^* \quad (2)$$

$$N(^2D) + O_2 \rightarrow NO + O \quad (3)$$

$$N(^4S) + O_2 \rightarrow NO + O \quad (4)$$

$$NO(v = 0) + O \rightarrow NO(v = 1) + O \ (\Delta E = -1875\ cm^{-1}) \quad (5a)$$

$$NO(v = 1) \rightarrow NO(v = 0) + h\nu_{5.3\mu m} \ (\Delta E = +1875\ cm^{-1}) \quad (5b)$$

$$NO(v = 1) + O \rightarrow NO(v = 0) + O \ (\Delta E = +1875\ cm^{-1}) \quad (5c)$$

$$NO + N(^4S) \rightarrow N_2 + O \quad (6)$$

The principal source of NO around the peak altitude of NO density (~110 km) is the chemical reaction between excited atomic $N(^2D)$ and $O_2$, and the dominant source of the NO above 120 km is the reaction of ground state atomic $N(^4S)$ and $O_2$, and the major sink of NO at all altitudes is its reaction with ground state atomic $N(^4S)$ (Barth, 1992). The lifetime of NO, which represents the lifetime against chemical reaction loss of NO in reaction with $N(^4S)$ at the amounts of $N(^4S)$ specified in WACCM-X, is up to 40 minutes, so the changes of NO can occur during the course of an eclipse. The blocking of solar radiation by the moon shadow during the eclipse induces a reduction in heating, photoionization, and photodissociation (Aplin et al., 2016), therefore, the population of energetic electrons decrease as well as temperature. Consequently, the amount of the excited state of atomic nitrogen ($N(^2D)$) decreases. The reduction of $N(^2D)$ directly affects Eq. (3) which is the most important source of NO at ~ 110 km (Barth, 1992). Moreover, Eq. (4) is the major source of NO above 120 km, and it is sensitive to the temperature (Barth, 1992). During the eclipse, the temperature decreases as shown in Figure 4(c). Since the reaction coefficient is sensitive to the temperature (Clark & Wayne, 1970), a lower temperature slows down the reaction rate of Eq. (4) and reduces the production of NO. Thus, NO concentration becomes smaller during the eclipse comparing to the non-eclipse reference (Figure 4(a)). In addition, since the NO concentration decreases with altitudes, the compressed atmosphere during solar eclipse causes the NO concentration depletion at the same altitude. Thus, the decrease of NO concentration is a combined effect of chemical processes and the atmospheric compression. Eq. (1) shows that NO concentration is proportional to the NO cooling rate, a decrease in NO concentration thus causes a decrease in NO cooling rate.

Note that the decrease of NO concentration is significant during the solar eclipse by ~8-15%, however, the relative change of the temperature is subtle, by only 1-3.5%. In the lower thermosphere, the NO cooling rate depends non-linearly on the neutral kinetic temperature according to $\exp(-\frac{h\nu_0}{k_B T_N})$, which is ~exp(-2700/$T_N$) (Kockarts, 1980), consequently, even a small disturbance in the temperature can cause a large NO cooling rate change. For example, at 160 km, the temperature decrease is ~ 18 K, and the non-eclipse reference temperature is 660 K. According to Eq. (1), the 18 K decrease of the temperature will cause ~ 10.9% decrease in the NO cooling rate. At 160 km, the decrease of NO cooling rate is 20.5% as shown in Figure 3(c), and the decrease of NO concentration is 11.8% (Figure 4(g)). Thus, temperature contributes to

nearly half of the NO cooling rate decrease. The temperature decrease is of equivalent importance in affecting the NO cooling rate during the solar eclipse. The eclipse-induced NO concentration and temperature decreases are the dominant drivers that cause the NO cooling rate decrease during the solar eclipse.

## 5 Summary

NO cooling rate changes during the December 14 2020 solar eclipse have been investigated in this paper via comparing SABER measurements and WACCM-X model simulations. We found the following:

(1) The NO cooling rate becomes larger below 122 km and smaller above 122 km during the solar eclipse than the non-eclipse reference. Between 130 km and 180 km, the reduction in NO cooling rate during the eclipse is larger than the 2-$\sigma$ standard deviation of the non-eclipse reference, indicating that there is more than 95% likelihood that the SABER observed eclipse-time NO cooling decrease is not due to the atmospheric natural variability.

(2) WACCM-X simulations show a decrease of NO cooling rate during the eclipse which is similar to the SABER measurements. The maximum decrease of NO cooling rate during the eclipse is 40% in SABER observations and is 25% in WACCM-X simulations. The SABER NO cooling rate is larger than the WACCM-X simulations during both the eclipse and the non-eclipse times.

(3) The NO cooling rate depends linearly on the NO and O densities and non-linearly on the temperature. The WACCM-X simulations show that the NO concentration decrease contributes to ~ 8-15% decrease in NO cooling rate and the temperature decrease contributes ~ 5-11% decrease in NO cooling rate. The eclipse-time NO concentration and temperature decreases are the major drivers and contribute about equally to the eclipse-time NO cooling rate decreases.

Future works including statistics of more case studies of the NO cooling rate variations during solar eclipses will be conducted when more SABER eclipse measurements are available.

## Acknowledgments

This work is supported by NASA Postdoctoral Program fellowship, and NSF AGS-1901126 and NASA AIM and TIMED/ SABER missions, NASA HSR Grants 80NSSC19K0835 and NNX17AI42G, and NASA NNX16AH06G, 80NSSC19K0278, and 80NSSC20K0189. Research was sponsored by the National Aeronautics and Space Administration (NASA) through a contract with ORAU. The views and conclusions contained in this document are those of the authors and should not be interpreted as representing the official policies, either expressed or implied, of the National Aeronautics and Space Administration (NASA) or the U.S. Government. The U.S. Government is authorized to reproduce and distribute reprints for Government purposes notwithstanding any copyright notation herein. The National Center for Atmospheric Research is sponsored by the National Science Foundation. For the WACCM-X simulations, we would like to acknowledge high-performance computing support from Cheyenne (doi:10.5065/D6RX99HX) provided by NCAR's Computational and Information Systems Laboratory, sponsored by the National Science Foundation.

## Open Research

The version 2.0 of the SABER data is used in this work. The SABER NO cooling rate data and the WACCM-X simulations shown in the paper are available are available at Zenodo at https://zenodo.org/record/6403832#.YkZmdzfMK-o.

## References

Aplin, K. L., Scott, C. J., & Gray, S. L. (2016). Atmospheric changes from solar eclipses. *Philosophical Transactions of the Royal Society A: Mathematical, Physical and Engineering Sciences*, *374*(2077), 20150217. https://doi.org/10.1098/rsta.2015.0217

Barth, C. A. (1992). Nitric oxide in the lower thermosphere. *Planetary and Space Science*, *40*(2), 315–336. https://doi.org/10.1016/0032-0633(92)90067-X

Barth, C. A. (2010). Joule heating and nitric oxide in the thermosphere, 2. *Journal of Geophysical Research: Space Physics*, *115*(A10). https://doi.org/10.1029/2010JA015565

412 Barth, C. A., Lu, G., & Roble, R. G. (2009). Joule heating and nitric oxide in the thermosphere. *Journal of*
413 *Geophysical Research: Space Physics*, *114*(A5). https://doi.org/10.1029/2008JA013765
414 Bharti, G., Sunil Krishna, M. V., Bag, T., & Jain, P. (2018). Storm Time Variation of Radiative Cooling by Nitric
415 Oxide as Observed by TIMED-SABER and GUVI. *Journal of Geophysical Research: Space Physics*,
416 *123*(2), 1500–1514. https://doi.org/10.1002/2017JA024576
417 Clark, I. D., & Wayne, R. P. (1970). Kinetics of the Reaction between Atomic Nitrogen and Molecular Oxygen in
418 the Ground (3sumg-) and First Excited (1Δ g) States. *Proceedings of the Royal Society of London Series A*,
419 *316*, 539–550. https://doi.org/10.1098/rspa.1970.0095
420 Curto, J. J., Heilig, B., & Piñol, M. (2006). Modeling the geomagnetic effects caused by the solar eclipse of 11
421 August 1999. *Journal of Geophysical Research: Space Physics*, *111*(A7).
422 https://doi.org/10.1029/2005JA011499
423 Dang, T., Lei, J., Wang, W., Zhang, B., Burns, A., Le, H., Wu, Q., Ruan, H., Dou, X., & Wan, W. (2018). Global
424 Responses of the Coupled Thermosphere and Ionosphere System to the August 2017 Great American Solar
425 Eclipse. *Journal of Geophysical Research: Space Physics*, *123*(8), 7040–7050.
426 https://doi.org/10.1029/2018JA025566
427 Dobbin, A. L., Aylward, A. D., & Harris, M. J. (2006). Three-dimensional GCM modeling of nitric oxide in the
428 lower thermosphere. *Journal of Geophysical Research: Space Physics*, *111*(A7).
429 https://doi.org/10.1029/2005JA011543
430 Duff, J. W., Dothe, H., & Sharma, R. D. (2003). On the rate coefficient of the N(2D)+O2→NO+O reaction in the
431 terrestrial thermosphere. *Geophysical Research Letters*, *30*(5). https://doi.org/10.1029/2002GL016720
432 Huba, J. D., & Drob, D. (2017). SAMI3 prediction of the impact of the 21 August 2017 total solar eclipse on the
433 ionosphere/plasmasphere system. *Geophysical Research Letters*, *44*(12), 5928–5935.
434 https://doi.org/10.1002/2017GL073549
435 Hurrell, J. W., Holland, M. M., Gent, P. R., Ghan, S., Kay, J. E., Kushner, P. J., Lamarque, J.-F., Large, W. G.,
436 Lawrence, D., Lindsay, K., Lipscomb, W. H., Long, M. C., Mahowald, N., Marsh, D. R., Neale, R. B.,
437 Rasch, P., Vavrus, S., Vertenstein, M., Bader, D., … Marshall, S. (2013). The Community Earth System
438 Model: A Framework for Collaborative Research. *Bulletin of the American Meteorological Society*, *94*(9),
439 1339–1360. https://doi.org/10.1175/BAMS-D-12-00121.1

Hwang, E. S., Castle, K. J., & Dodd, J. A. (2003). Vibrational relaxation of NO(v = 1) by oxygen atoms between 295 and 825 K. *Journal of Geophysical Research: Space Physics*, *108*(A3). https://doi.org/10.1029/2002JA009688

Kinnison, D. E., Brasseur, G. P., Walters, S., Garcia, R. R., Marsh, D. R., Sassi, F., Harvey, V. L., Randall, C. E., Emmons, L., Lamarque, J. F., Hess, P., Orlando, J. J., Tie, X. X., Randel, W., Pan, L. L., Gettelman, A., Granier, C., Diehl, T., Niemeier, U., & Simmons, A. J. (2007). Sensitivity of chemical tracers to meteorological parameters in the MOZART-3 chemical transport model. *Journal of Geophysical Research: Atmospheres*, *112*(D20). https://doi.org/10.1029/2006JD007879

Knipp, D. J., Pette, D. V., Kilcommons, L. M., Isaacs, T. L., Cruz, A. A., Mlynczak, M. G., Hunt, L. A., & Lin, C. Y. (2017). Thermospheric nitric oxide response to shock-led storms. *Space Weather*, *15*(2), 325–342. https://doi.org/10.1002/2016SW001567

Kockarts, G. (1980). Nitric oxide cooling in the terrestrial thermosphere. *Geophysical Research Letters*, *7*(2), 137–140. https://doi.org/10.1029/GL007i002p00137

Le, H., Liu, L., Yue, X., & Wan, W. (2008). The midlatitude F2 layer during solar eclipses: Observations and modeling. *Journal of Geophysical Research: Space Physics*, *113*(A8). https://doi.org/10.1029/2007JA013012

Lei, J., Burns, A. G., Thayer, J. P., Wang, W., Mlynczak, M. G., Hunt, L. A., Dou, X., & Sutton, E. (2012). Overcooling in the upper thermosphere during the recovery phase of the 2003 October storms. *Journal of Geophysical Research: Space Physics*, *117*(A3). https://doi.org/10.1029/2011JA016994

Lei, J., Dang, T., Wang, W., Burns, A., Zhang, B., & Le, H. (2018). Long-Lasting Response of the Global Thermosphere and Ionosphere to the 21 August 2017 Solar Eclipse. *Journal of Geophysical Research: Space Physics*, *123*(5), 4309–4316. https://doi.org/10.1029/2018JA025460

Lei, J., Thayer, J. P., Lu, G., Burns, A. G., Wang, W., Sutton, E. K., & Emery, B. A. (2011). Rapid recovery of thermosphere density during the October 2003 geomagnetic storms. *Journal of Geophysical Research: Space Physics*, *116*(A3). https://doi.org/10.1029/2010JA016164

Li, Z., Knipp, D., & Wang, W. (2019). Understanding the Behaviors of Thermospheric Nitric Oxide Cooling During the 15 May 2005 Geomagnetic Storm. *Journal of Geophysical Research: Space Physics*, *124*(3), 2113–2126. https://doi.org/10.1029/2018JA026247

Liu, H.-L., Bardeen, C. G., Foster, B. T., Lauritzen, P., Liu, J., Lu, G., Marsh, D. R., Maute, A., McInerney, J. M., Pedatella, N. M., Qian, L., Richmond, A. D., Roble, R. G., Solomon, S. C., Vitt, F. M., & Wang, W. (2018). Development and Validation of the Whole Atmosphere Community Climate Model With Thermosphere and Ionosphere Extension (WACCM-X 2.0). *Journal of Advances in Modeling Earth Systems*, *10*(2), 381–402. https://doi.org/10.1002/2017MS001232

Liu, J., Liu, H., Wang, W., Burns, A. G., Wu, Q., Gan, Q., Solomon, S. C., Marsh, D. R., Qian, L., Lu, G., Pedatella, N. M., McInerney, J. M., Russell, J. M., & Schreiner, W. S. (2018). First Results From the Ionospheric Extension of WACCM-X During the Deep Solar Minimum Year of 2008. *Journal of Geophysical Research: Space Physics*, *123*(2), 1534–1553. https://doi.org/10.1002/2017JA025010

Lu, G., Mlynczak, M. G., Hunt, L. A., Woods, T. N., & Roble, R. G. (2010). On the relationship of Joule heating and nitric oxide radiative cooling in the thermosphere. *Journal of Geophysical Research: Space Physics*, *115*(A5). https://doi.org/10.1029/2009JA014662

McInerney, J. M., Marsh, D. R., Liu, H.-L., Solomon, S. C., Conley, A. J., & Drob, D. P. (2018). Simulation of the 21 August 2017 Solar Eclipse Using the Whole Atmosphere Community Climate Model-eXtended. *Geophysical Research Letters*, *45*(9), 3793–3800. https://doi.org/10.1029/2018GL077723

Mlynczak, M. G. (1997). Energetics of the mesosphere and lower thermosphere and the SABER experiment. *Advances in Space Research*, *20*(6), 1177–1183. https://doi.org/10.1016/S0273-1177(97)00769-2

Mlynczak, M. G., Hunt, L. A., Lopez-Puertas, M., Funke, B., Emmert, J., Solomon, S., Yue, J., Russell, J. M., & Mertens, C. (2021). Spectroscopy, gas kinetics, and opacity of thermospheric nitric oxide and implications for analysis of SABER infrared emission measurements at 5.3 μm. *Journal of Quantitative Spectroscopy and Radiative Transfer*, *268*, 107609. https://doi.org/10.1016/j.jqsrt.2021.107609

Mlynczak, M. G., Hunt, L. A., Marshall, B. T., Martin-Torres, F. J., Mertens, C. J., Russell, J. M., Remsberg, E. E., López-Puertas, M., Picard, R., Winick, J., Wintersteiner, P., Thompson, R. E., & Gordley, L. L. (2010). Observations of infrared radiative cooling in the thermosphere on daily to multiyear timescales from the TIMED/SABER instrument. *Journal of Geophysical Research: Space Physics*, *115*(A3). https://doi.org/10.1029/2009JA014713

Mlynczak, M. G., Martin-Torres, F. J., Crowley, G., Kratz, D. P., Funke, B., Lu, G., Lopez-Puertas, M., Russell, J. M., Kozyra, J., Mertens, C., Sharma, R., Gordley, L., Picard, R., Winick, J., & Paxton, L. (2005). Energy

transport in the thermosphere during the solar storms of April 2002. *Journal of Geophysical Research: Space Physics*, *110*(A12). https://doi.org/10.1029/2005JA011141

Mlynczak, M. G., Martin-Torres, F. J., & Russell, J. M. (2007). Correction to "Energy transport in the thermosphere during the solar storms of April 2002." *Journal of Geophysical Research: Space Physics*, *112*(A2). https://doi.org/10.1029/2006JA012008

Mlynczak, M., Martin-Torres, F. J., Russell, J., Beaumont, K., Jacobson, S., Kozyra, J., Lopez-Puertas, M., Funke, B., Mertens, C., Gordley, L., Picard, R., Winick, J., Wintersteiner, P., & Paxton, L. (2003). The natural thermostat of nitric oxide emission at 5.3 μm in the thermosphere observed during the solar storms of April 2002. *Geophysical Research Letters*, *30*(21). https://doi.org/10.1029/2003GL017693

Murphy, R. E., Lee, E. T. P., & Hart, A. M. (1975). Quenching of vibrationally excited nitric oxide by molecular oxygen and nitrogen. *The Journal of Chemical Physics*, *63*(7), 2919–2925. https://doi.org/10.1063/1.431701

Richards, P. G. (2004). On the increases in nitric oxide density at midlatitudes during ionospheric storms. *Journal of Geophysical Research: Space Physics*, *109*(A6). https://doi.org/10.1029/2003JA010110

Russell, J., Mlynczak, M., Gordley, L., Tansock, J., & Esplin, R. (1999). An Overview of the SABER Experiment and Preliminary Calibration Results. *Proceedings of SPIE*, *3756*, 277–288. https://doi.org/10.1117/12.366382

Sharma, R. D., Dothe, H., & Duff, J. W. (1998). Model of the 5.3 μm radiance from NO during the sunlit terrestrial thermosphere. *Journal of Geophysical Research: Space Physics*, *103*(A7), 14753–14768. https://doi.org/10.1029/98JA00896

Sheng, C., Lu, G., Solomon, S. C., Wang, W., Doornbos, E., Hunt, L. A., & Mlynczak, M. G. (2017). Thermospheric recovery during the 5 April 2010 geomagnetic storm. *Journal of Geophysical Research: Space Physics*, *122*(4), 4588–4599. https://doi.org/10.1002/2016JA023520

Siskind, D. E., Barth, C. A., Evans, D. S., & Roble, R. G. (1989). The response of thermospheric nitric oxide to an auroral storm: 2. Auroral latitudes. *Journal of Geophysical Research: Space Physics*, *94*(A12), 16899–16911. https://doi.org/10.1029/JA094iA12p16899

522 Zhang, Y., Paxton, L. J., Morrison, D., Marsh, D., & Kil, H. (2014). Storm-time behaviors of O/N2 and NO
523 variations. *Journal of Atmospheric and Solar-Terrestrial Physics*, *114*, 42–49.
524 https://doi.org/10.1016/j.jastp.2014.04.003
525

**Figure 6.**

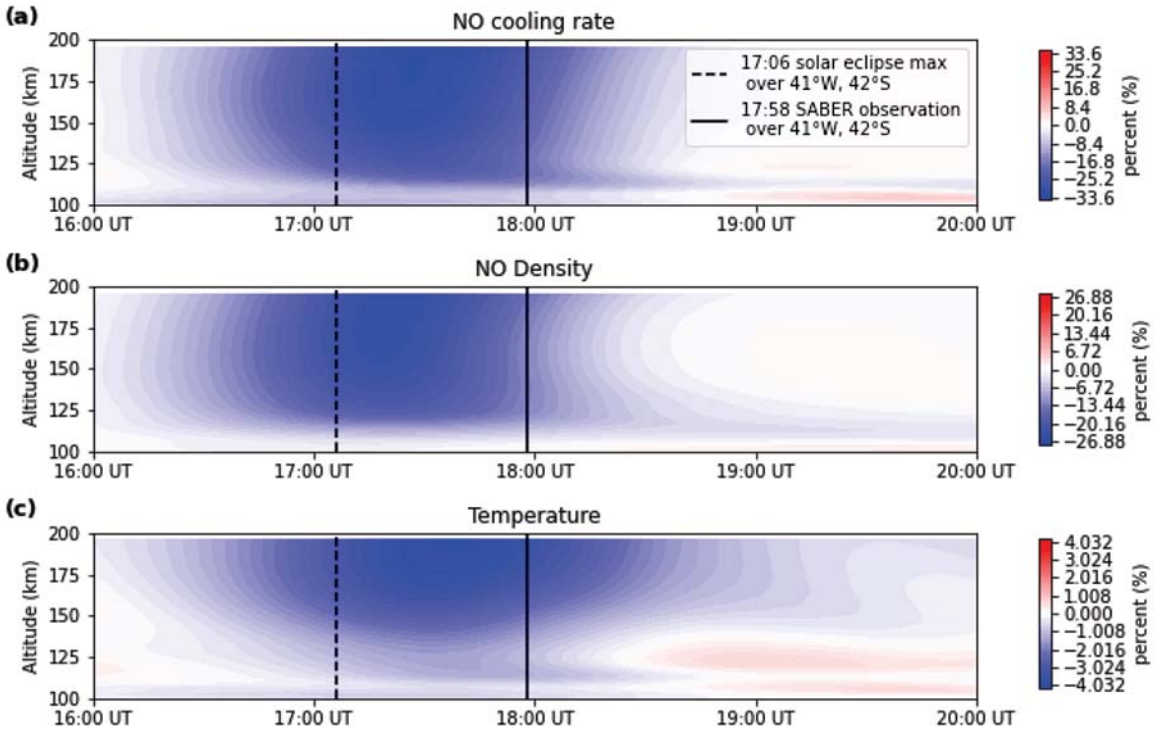
(a)
NO cooling rate
Altitude (km)
200
175
150
125
100
16:00 UT
17:00 UT
18:00 UT
19:00 UT
20:00 UT
17:06 solar eclipse max over 41°W, 42°S
17:58 SABER observation over 41°W, 42°S
33.6
25.2
16.8
8.4
0.0
−8.4
−16.8
−25.2
−33.6
percent (%)
(b)
NO Density
26.88
20.16
13.44
6.72
0.00
−6.72
−13.44
−20.16
−26.88
percent (%)
(c)
Temperature
4.032
3.024
2.016
1.008
0.000
−1.008
−2.016
−3.024
−4.032
percent (%)

**Figure 3.**

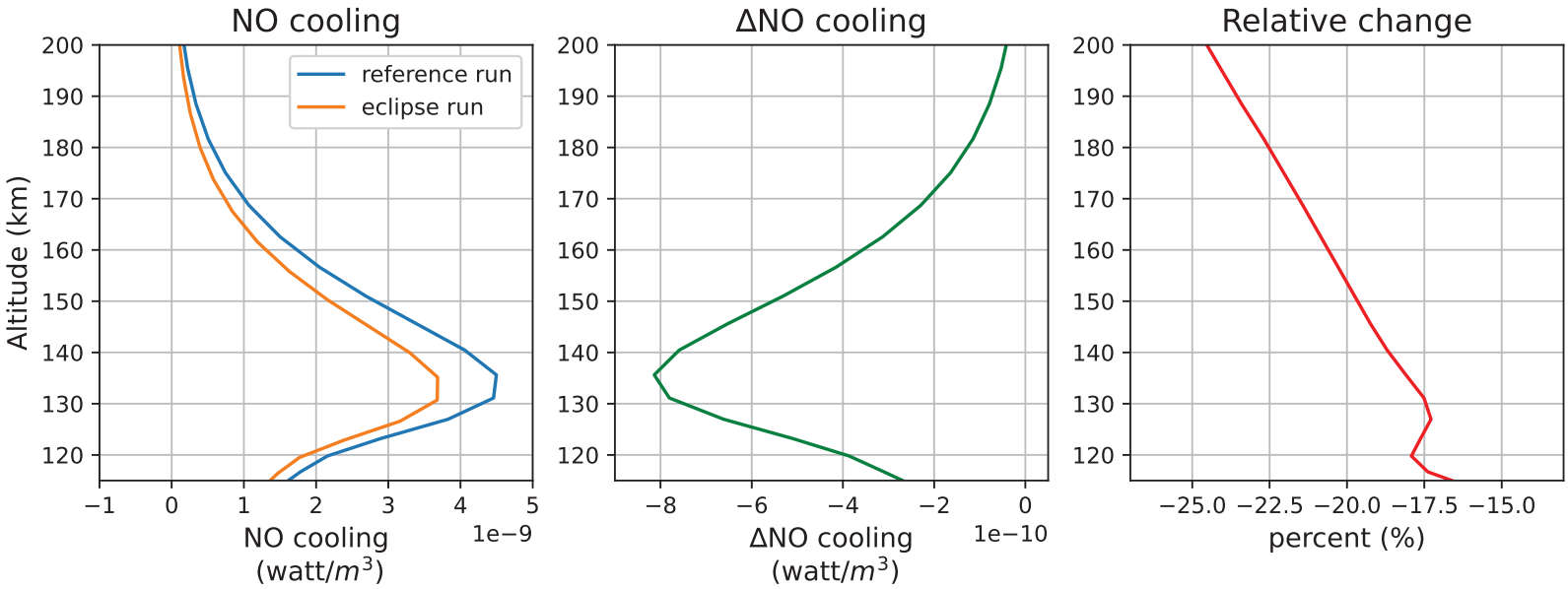
NO cooling
ΔNO cooling
Relative change
reference run
eclipse run
Altitude (km)
200
190
180
170
160
150
140
130
120
−1
0
1
2
3
4
5
1e−9
NO cooling
(watt/$m^3$)
−8
−6
−4
−2
0
1e−10
ΔNO cooling
(watt/$m^3$)
−25.0
−22.5
−20.0
−17.5
−15.0
percent (%)

**Figure 2.**

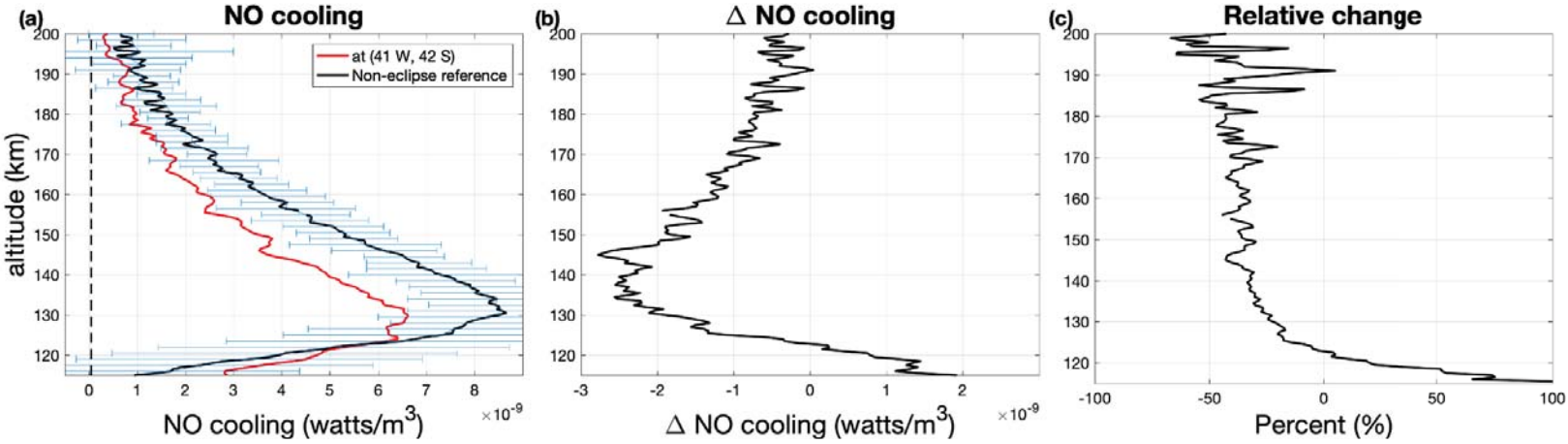
(a)
NO cooling
at (41 W, 42 S)
Non-eclipse reference
altitude (km)
NO cooling (watts/m3)
×10-9
(b)
Δ NO cooling
Δ NO cooling (watts/m3)
×10-9
(c)
Relative change
Percent (%)

**Figure 4.**

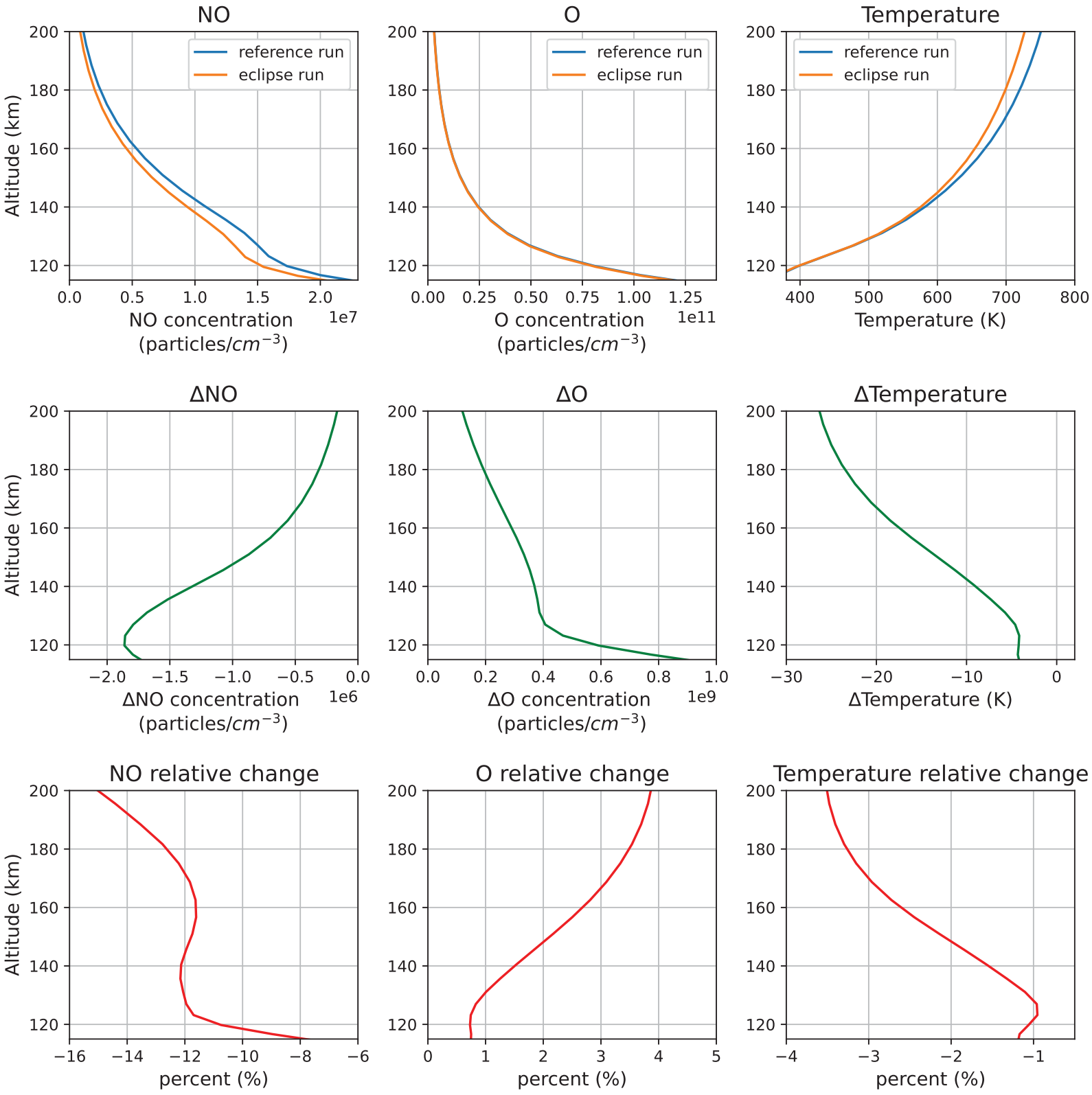
NO
reference run
eclipse run
Altitude (km)
200
180
160
140
120
0.0
0.5
1.0
1.5
2.0
1e7
NO concentration
(particles/$cm^{-3}$)
O
reference run
eclipse run
0.00
0.25
0.50
0.75
1.00
1.25
1e11
O concentration
(particles/$cm^{-3}$)
Temperature
reference run
eclipse run
400
500
600
700
800
Temperature (K)
ΔNO
−2.0
−1.5
−1.0
−0.5
0.0
1e6
ΔNO concentration
(particles/$cm^{-3}$)
ΔO
0.0
0.2
0.4
0.6
0.8
1.0
1e9
ΔO concentration
(particles/$cm^{-3}$)
ΔTemperature
−30
−20
−10
0
ΔTemperature (K)
NO relative change
−16
−14
−12
−10
−8
−6
percent (%)
O relative change
0
1
2
3
4
5
percent (%)
Temperature relative change
−4
−3
−2
−1
percent (%)

**Figure 5.**

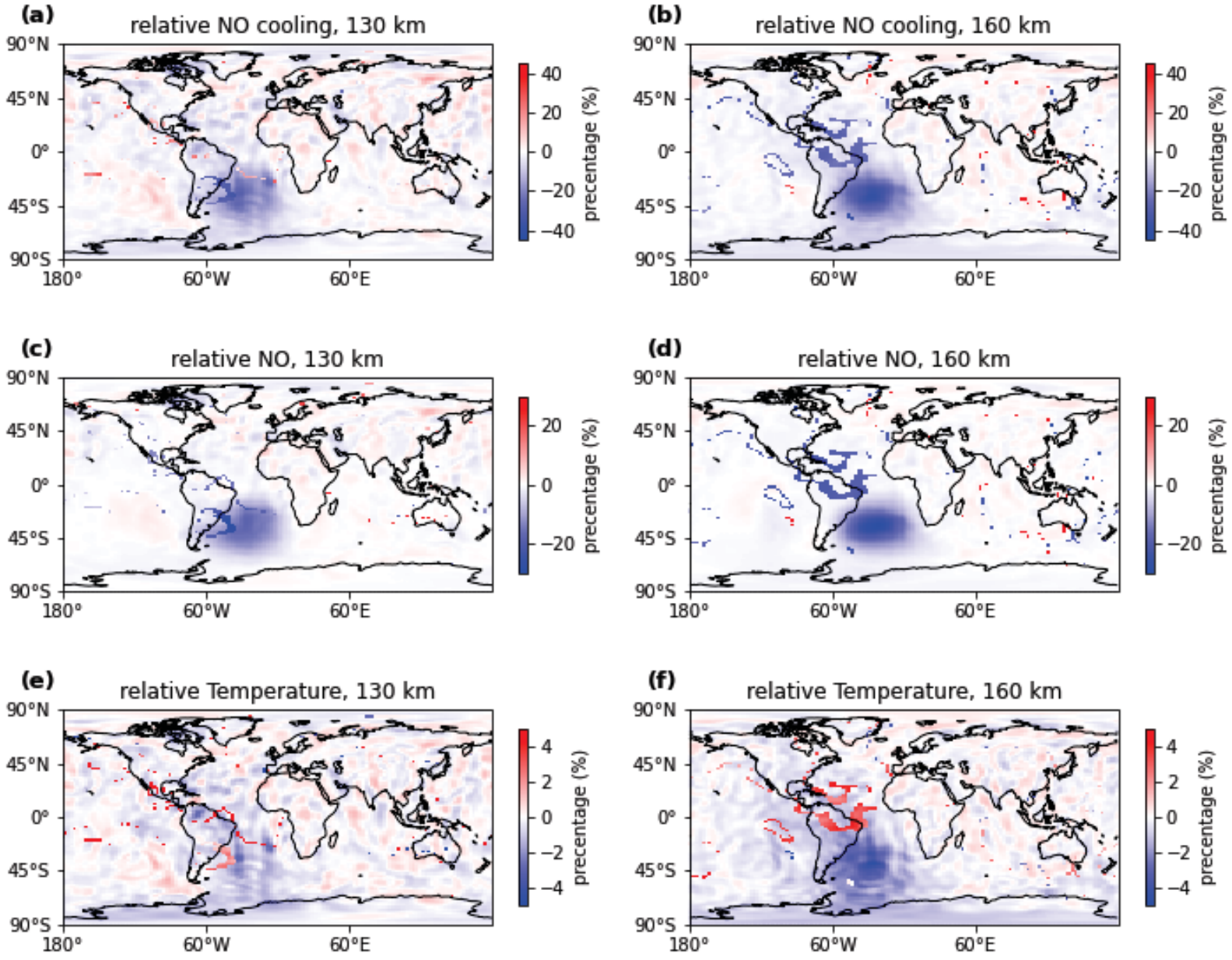
(a)
relative NO cooling, 130 km
(b)
relative NO cooling, 160 km
(c)
relative NO, 130 km
(d)
relative NO, 160 km
(e)
relative Temperature, 130 km
(f)
relative Temperature, 160 km
90°N
45°N
0°
45°S
90°S
180°
60°W
60°E
precentage (%)
40
20
0
−20
−40
4
2
−2
−4

**Figure 1.**

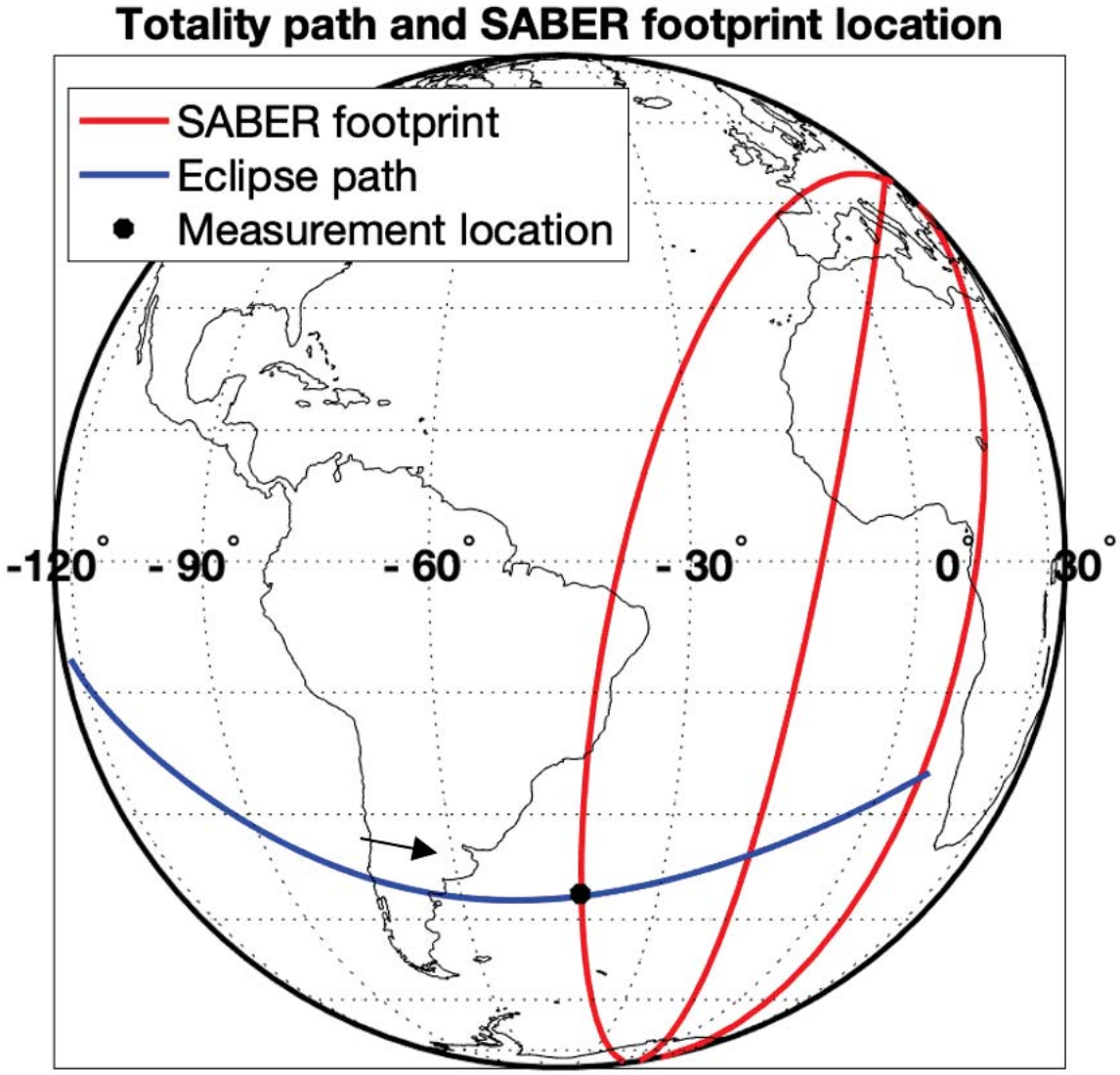
Totality path and SABER footprint location
SABER footprint
Eclipse path
Measurement location
-120°
- 90°
- 60°
- 30°
0°
30°